Wireless position sensing and normalization of embedded resonant sensors using a resonator array

By
Yee Jher Chan[1], Adam R. Carr[1], Sadaf Charkhabi[1], Mason Furnish[1], Andee M. Beierle[1], and Nigel F. Reuel[1*]

1. Department of Chemical and Biological Engineering, Iowa State University

*Corresponding Author – reuel@iastate.edu

Abstract

In this work, four square, planar resonators with unique frequency windows were used to form a 2 by 2 array for wireless position determination and normalization of position-dependent, embedded resonant sensors. First, a master table of S|21| gain and phase data was collected at 8100 positions. Automated scripts extracted the characteristic gain and phase peaks and used cubic interpolation to expand the master table to 7,157,160 unique angle and coordinate positions. An unknown position is then determined by comparing its S|21| measurements to this table. To further improve the position accuracy, multiple measurements are collected on linear flyby trajectories. The average and standard deviation of predicted position offset from true value using this method were 3.2 and 2.3 mm, respectively. To test normalization of a position dependent sensor, a spiral resonant sensor was placed underneath the square array. The sensor signal was modulated using varying amounts of water on the sensor surface. A corrected reading was determined using four different flyby trajectories using the position array data to adjust the signal based on position. We found that average errors of the normalized signals were between 0.04 to 0.15 MHz at lower water volume (0.5 mL) and -0.53 to -0.74 MHz at higher water volume (2.0 mL). In its current state, the positional array can be used for asset tracking or feedback control and the sensor normalization can be used to improve the measurement accuracy of embedded sensors. This can technique can be further improved by collecting more accurate master calibration data using an automated system.

Introduction

Resonant sensors, also known as LC sensors or LCR tanks, have been used in many applications such as wireless monitoring of temperatures [1], [2], pressures [3], [4], dielectrics [5], [6], and enzyme activities [7]. They are composed of an inductor (L) and capacitor (C) which tune the circuit to resonate at a specific frequency. Upon interaction or activity of the analyte, the inductance and/or capacitance of the circuit modulates and the response is reported in a shift or attenuation of the resonant signal [8]. The resonant signal can be interrogated wirelessly using a vector network analyzer, observing the one-port (S_{11}) or two-port (S_{21}) scattering parameters (magnitude and phase of RF signal over a set frequency range). Typically these are very large, expensive benchtop units [8], [9]. Because the resonator is energized by the vector

network analyzer antennas *via* near-field coupling, there is no need for on-board power; however, the read range is typically limited to the <10 cm range [10]. The use of a periodic array can improve this read range [9]. If the resonators are tuned to the sub-microwave range (especially <150 Mhz), they have the added benefit of penetration into aqueous and biological systems [11], thus allowing for embedded sensors in traditionally opaque systems such as tissue [12], soil [13], and plastic parts [14].

One limitation of resonant sensors is the high-degree of positional sensitivity between the vector network analyzer reader antennas and the resonator. The scattering parameters and resonant frequency response are dependent upon the mutual inductance which is a function of the system geometry and separation distance [15]. All studies to date mitigate this problem by fixing the reader and resonant sensor in place or ensuring that they return to the same position via mechanical or optical alignment marks [6], [13], [14]. For example, a recent work demonstrated the ability to wirelessly measure alignment angle and angular velocity using a split ring resonator, but the method requires the X and Y positions to be fixed [16]. This works for static systems, or systems which allow for installation of positional cues, however there is no solution for systems which are completely embedded and do not allow for careful repositioning. An example of such a system would be resonant sensors embedded in the ground to measure the hydrolytic activity of soils in which an agronomist or tractor would return to the proximal site of the sensor and take a reading [13]. Without any method of position-based normalization, the user would not know if an observed signal shift was due to a change in the sensor or a change in the position of the reader in relation to the embedded sensor.

It is the purpose of this work to overcome this long-standing limitation through the design and demonstration of an array of resonators, that can be embedded with the resonant sensor and 1) provide positional feedback in a closed system and 2) allow for normalization of the resonant sensor. First, positional sensing is demonstrated using a 2x2 array of resonators fabricated with resonant frequencies in the 25-100 MHz range. These frequencies were chosen to match a low-cost portable VNA capable of measuring 0.1 to 180 MHz, which leaves the 100-180 MHz range for the resonant sensor response. Linear flyby paths with six measurements in the range of the array are then used to improve the spatial predictions. The spatial predictions are then used to normalize the response of a central resonant sensor, tuned to respond to volume of water, that is embedded with the array. Finally, next steps and intended applications of this work are discussed.

Results and Discussion

To test position sensing using an embedded resonator array, an acrylic sheet was placed above four resonators at a step-off distance of 6 mm (Fig 1). The sheet was patterned with a 14x14 cm major grid with 1 mm minor tick lines (using a laser cutter) to enable accurate reader placement. A handheld, two-port vector network analyzer with a custom co-planar two loop coil reader (Fig 1c) is then used to measure the transmission scattering parameters, S_{21} gain and phase, as the sensor response (Fig 1d). Top and bottom peaks of the signals reflected the resonant peaks of each coil. These were extracted through custom MATLAB scripts (Supplement 1). Each of the four positional resonators were tuned to have a set resonant frequency in the 25-100MHz range with no overlap of their signals (Fig 1d).

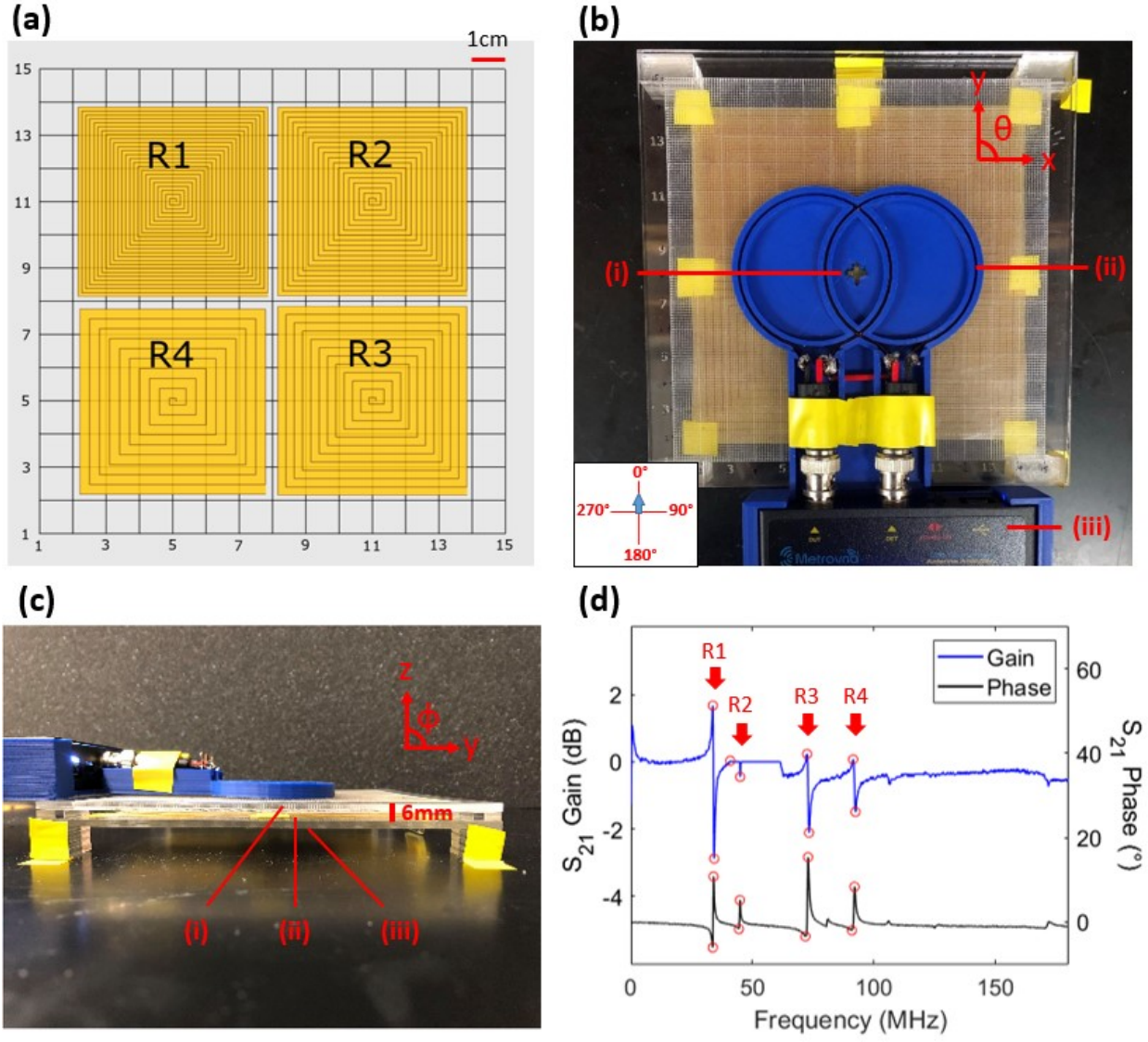

Figure 1 – Depiction of resonator array for positional sensing. (a) Four resonators with unique, non-overlapping resonant frequencies in the range of 25 to 100 MHz are positioned in a 2x2 grid on the bottom of a 14x14 cm acrylic reading grid (3mm thickness). (b) Photo of top-view of experimental setup

showing resonator array below the transparent grid; the '+' shaped window at the center of the reader (i) is used to position on the grid; also visible, are the two coplanar loop reader antennas (ii) affixed to the handheld vector network analyzer (iii). Inset shows the reader's angular direction. (c) Photo of side-view of reading system; the 6mm displacement between the reading coils and the resonant sensors is shown which is composed of (i) 3 mm acrylic as support frame and grid for taking measurement, (ii) 3mm air gap and (iii) acrylic base with resonators secured on top. (d) Example reader response, showing two-port scattering response (S_{21} gain and phase) of the four resonators showing the distinct resonant peaks of each.

The transmission scattering parameter (S_{21}) phase and gain result from mutual inductance (*M*) coupling between the reader and coil; it is expressed as follows [17]:

$$M = k\sqrt{L_r L_s} \tag{1}$$

where k is the coupling coefficient, L_r is the inductance of the reader coil, and L_s is the inductance of sensor. During interrogation, the measured impedance on the reader terminal resulting from the sensor is [17]:

$$Z = \frac{\omega^2 M^2}{Z_s} \tag{2}$$

Where ω is the interrogation frequency (in radians) and Z_s is the intrinsic impedance of the sensor. As the position of reader changes, the coupling coefficient (k) between the reader and sensor changes, and therefore the mutual inductance and measured impedance. The gain is a measure of power of electromagnetic waves transmitted between ports of the VNA and is dependent on impedance. Thus the magnitude of the S_{21} parameter is directly affected by varying the reader position (x, y, θ, etc).

In terms of the phase data, the local minimum of the phase dip can be approximated by [18]

$$\Delta\varphi \cong \tan^{-1}(k^2 Q) \tag{3}$$

Where k is the coupling coefficient and Q is the quality factor. Again, the phase magnitude is dependent on the coupling coefficient, and thus changes with position as well. In this manner the gain and phase magnitudes can be used as signal features to help determine the position of the reader.

For a single resonator, there exist many positions where the coupling between reader and sensor result in similar gain and phase features. Thus with a single resonator we are unable to differentiate all positions. Orthogonal feature information is provided by using a sensor array, thus allowing for higher level position prediction. Measurements that are lacking signals from other sensors in the array further narrow the possible positions. When designing the sensor array, square resonators were used (Fig 1a) and were placed close enough to each other to provide a continuous area for measurements that was larger than the reader coils. We found that when circular, Archimedean spiral resonators were used for the array or when the coils

were not placed close enough to each other that we observed multiple 'dead zones' where no signals are detected within the array; this confounds our ability to predict position.

Our method to predict the position of the reader is based on interpolating from a master database of array measurements. Readings were taken at every 1 cm interval from 1 to 15 cm in the x-y direction and at 10° intervals in the angular (θ) direction (Fig 2a) across the array. This resulted in 8100 unique measurements to build the database. The gain and phase peak magnitudes were then extracted from each measurement using our custom algorithms and stacked into a master plot to determine cut-offs for each resonator (Fig 2b). Since four resonators were used, four frequency regions with significant peaks were observed. The magnitude of the most significant peak within each frequency region was then saved for each coordinate and angle combination. We then created a finer grid of position and angular measurements through cubic interpolation, forming 0.1 cm intervals in x-y direction and 1° intervals in θ direction (Fig 2c) that resulted in 7,157,160 possible position and angle combinations. This fine-grid, master data is then saved and used for predicting positions from new measurements (see Methods section and Supplement 1 for more detail). In brief, the method of predicting the position of an unknown sample proceeds similarly. First, the reader is placed somewhere on the array and the S_{21} gain and phase data are collected (Fig 2d). The magnitude of the most significant peak at each frequency region defined from the master plot (Fig 2b) are extracted (Fig 2e). These values are then compared to the interpolated master data table to find the coordinates that contain the smallest error between measured and predicted; this results in rank ordered predictions with the top predictions very closely matching the measured position, in most cases (Figure 2f).

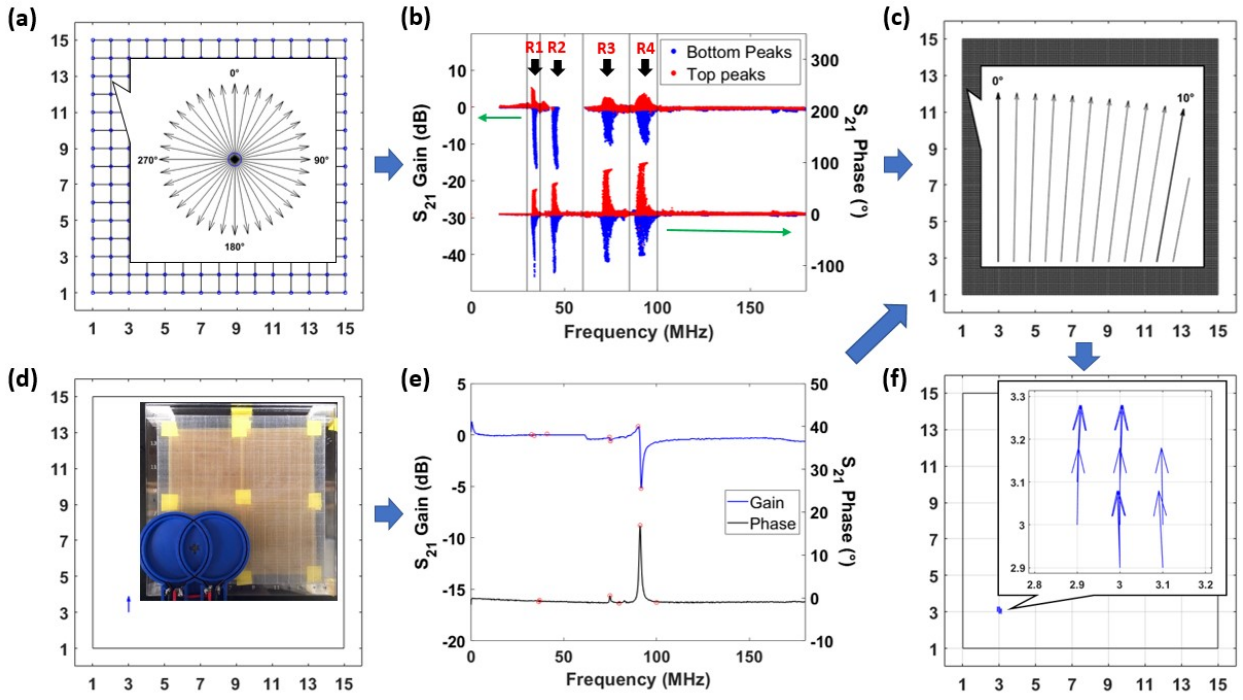

Figure 2 – Method for determining reader position. (a) Coordinate system of experimental setup where data are collected at intervals of 1 cm in x and y direction (1 to 15) and 10° in θ direction (0° to 350°). (b) Stacked plot of gain and phase peaks extracted from all data collected in (a) showing the 4 distinct resonator response ranges. (c) Interpolated coordinate system with intervals of 0.1cm in x-y direction and 1 ° in θ direction. (d) A schematic of a sample taken at (3, 3) and 0°. (e) Signal obtained from (d) where the top and bottom peaks are marked with red circles from the automated peak finding algorithm. (f) Best of 10 predicted positions after comparing (e) to (c) and minimizing squared errors.

Before discussing the accuracy of this approach, we must make a brief note on harmonic signals that arise from resonators. The harmonics arise from higher frequency modes which display peaks at roughly integer multiples of the fundamental frequency. For this method to work, non-overlapping frequency regions for the peaks is crucial to distinguish between the arrayed resonators. However, it is possible that a resonator could have its harmonic peaks overlapping into frequency regions of others in the array. Fortunately, the magnitude of these harmonic peaks are smaller (less than 2dB in gain and less than 13° in phase) compared to the primary peaks. Thus by selecting the most significant peak (highest magnitude) that is measured in each frequency region we avoid selecting the harmonic peaks. The harmonic frequencies can also be dampened by placing a rigid substrate such as acrylic or polystyrene between the resonator and the reader antennas (Supplement 2).

Algorithm accuracy

To examine the accuracy of the position predicting algorithm, 35 representative, random samples were taken within the 14x14 cm measurement region (Figure 3a). The errors between the measured features and the interpolated master table data were rank ordered. The actual values were found to always lie within the top 1% of the rank ordered 7,157,160 possible positions, with an average percentile of 0.035% (Fig 3b) with percentile being calculated as:

$$\text{Percentile} = \frac{\text{index of the actual coordinate in the sorted errors}}{\text{total number of coordinates } (= 7{,}157{,}160)}$$

The predicted angle found by minimum error was not always the angle of the actual measurement; however, when we compare the ranking for all coordinates at the predicted *vs.* actual angle they are similar; this can be readily visualized with error heat maps (Fig 3c) where the z-dimension is the rank order percentile (< 1% being close to top of rank order list and 99% being bottom of rank order according to error). The darker blue regions represent the coordinates with lower error, therefore indicating higher probability regions where the measurement was taken.

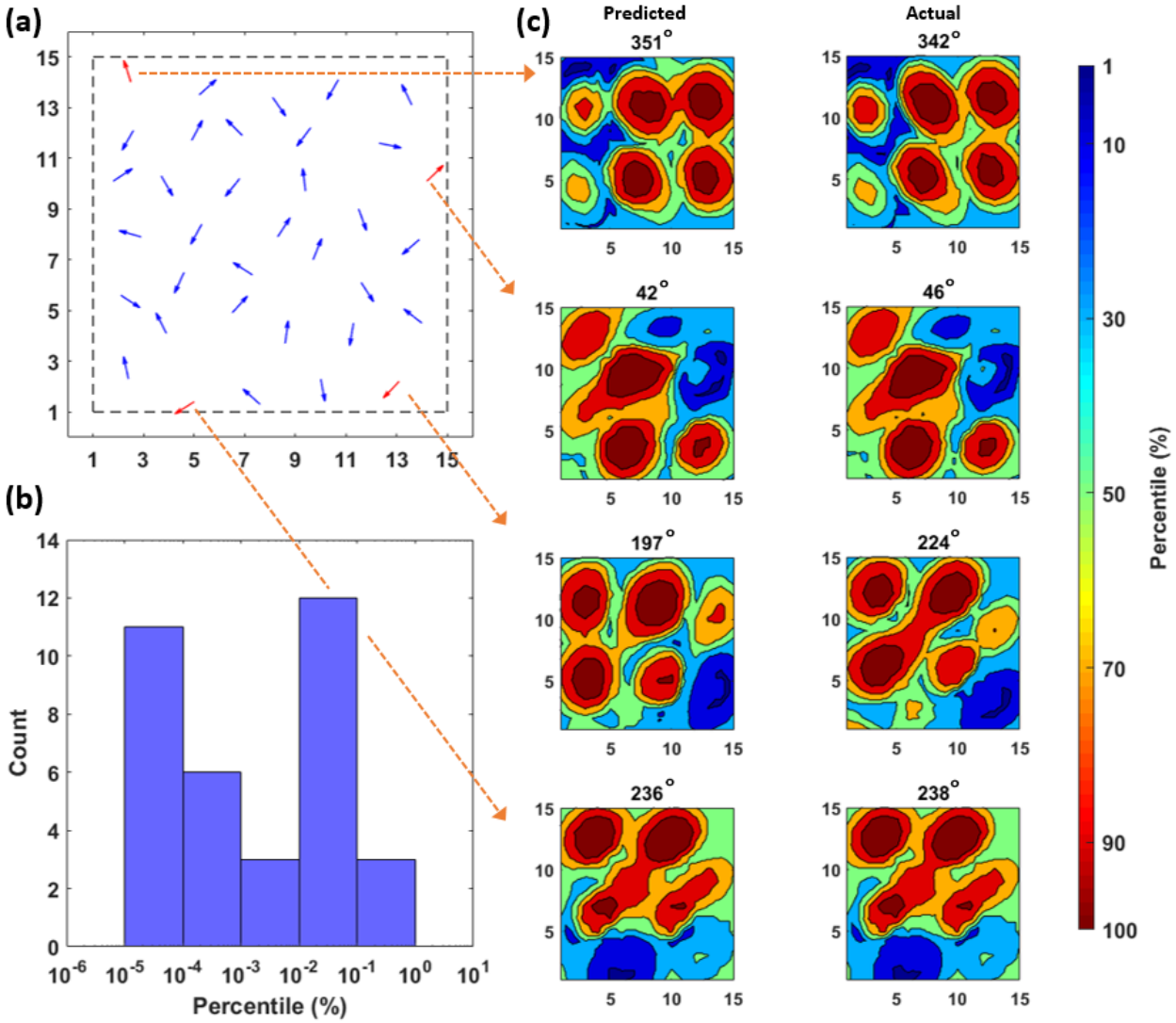

Figure 3 – Determining positional accuracy. (a) Coordinates of 35 randomly taken samples within the measurement area of the resonator array. (b) Histogram of ranking percentiles for the 35 samples, with smaller percentile denoting the actual coordinate being higher on the rank order list. (c) Comparing predicted angle error rankings and actual angle error rankings (low percentile is small error difference, and vice versa) for four different points showing that regions of most likely position (dark blue) are similar.

Flyby Linear Trajectory

Although the static array technique above was able to narrow down the actual position to <1% of the possible coordinates in the master interpolated table, this can be further improved by combining multiple measurements. The prediction is improved by taking samples along a linear trajectory, pooling information from the top 2000 predictions (top 0.03%) from each measured point and finding the best fit line. To test this idea, six samples were taken along each

trajectory, for a total of eight different trajectories (Figure 4a). Finding the best fit line is detailed in methods below, but in brief, a line is drawn through one predicted position using the θ found for that position. Then, all the top X and Y positions at each of the other 5 samples locations (2000 at each location) are compared to this line, and the closest X, Y coordinates for each are recorded. This is done for all 2000 points for each of the six measurements along the line (12,000 iterations). The most frequently recorded X, Y position at each sampling location is then found. A line is fit through these 6 points (using least squares regression) and the final predicted positions at each location were then selected to fall on this line. We found this ranking method to be more accurate than simply fitting a line through all the top predicted points (12,000), as this latter method placed undue bias on those points which are obviously not on the same path (poorer predictions). The resulting best fit lines from our eight experiments are drawn as dashed arrows in Fig. 4a. By comparing the best fit points determined from this flyby fitting algorithm to actual positions, we are able to find the probability distribution for offset error, or difference between final predicted position and actual position (Fig 4b). An asymmetric distribution that includes skew, such as the Weibull distribution fits this data better than a normal distribution; this takes into account the stochastic events of higher error, sources of which are discussed below. The fit distribution shows that 95% of all measurements have an error smaller than 7.5 mm. We also determine that the mean and standard deviation are 3.2 and 2.3 mm, respectively (Figure 4b). Moreover, we find that the angle error and average distance between the actual trajectory and best-fit to be less than 1.52° and 1.6 mm, respectively.

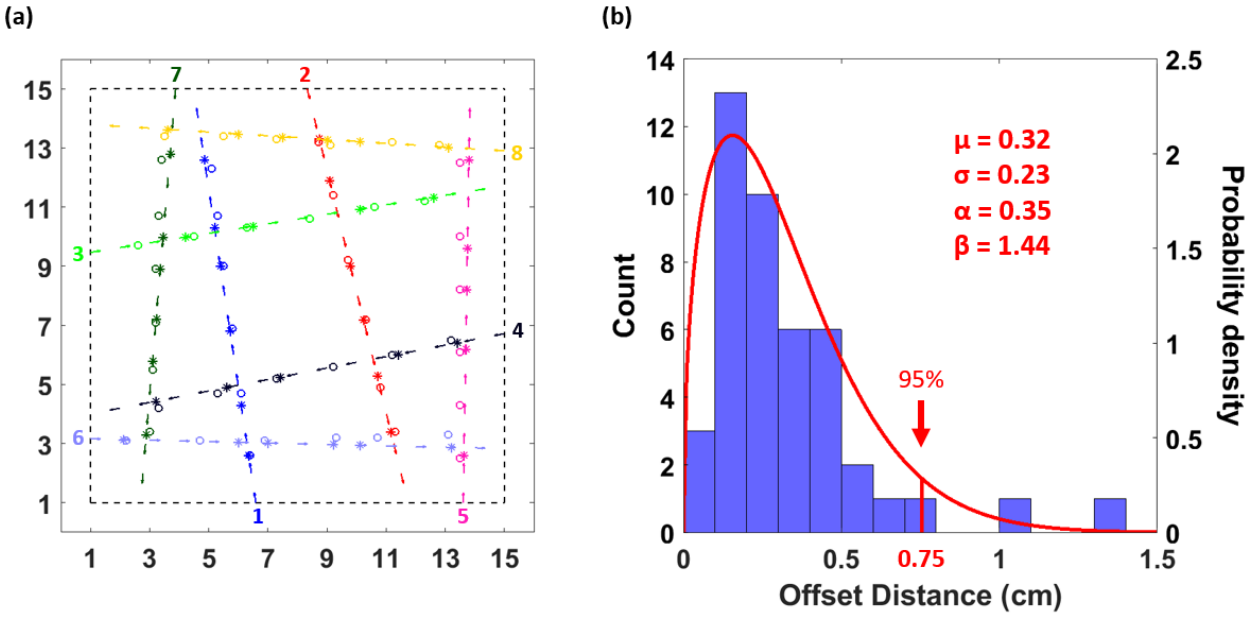

Figure 4 – Flyby trajectory fidelity. (a) Eight linear trajectories showing coordinates where reading was taken, predicted coordinates, and predicted path of the reader denoted by empty-filled markers, star

markers, and arrow lines, respectively. (b) Histogram of the distance between predicted and actual coordinates as well as probability density function fit (Weibull distribution with statistics and fit parameters for this distribution shown in red, where μ = mean, σ = standard deviation, and α and β = are Weibull parameters).

Table 1 – Comparison of angle and average distance between the actual and predicted path of trajectory.

Trajectory	Actual Angle	Predicted Angle	Average distance between lines (cm)
1	352	351	0.1186
2	166	166	0.0597
3	81	81	0.0402
4	256	259	0.1250
5	0	1	0.4453
6	272	274	0.1208
7	182	185	0.1611
8	89	91	0.1979

We attribute most of this offset error to come from limitations caused by manual data collection. The collected data on which this algorithm is founded is only composed of 2,000 manually collected entries. Each of these have a small source of error as the reader cannot be perfectly positioned on the grid by hand (roughly a tolerance of ±1 mm in x-y direction and ±2° in θ). This results in a poorer interpolated master grid, and thus poorer predictions from the algorithm. This could be improved by automating the master grid data (using a programmed XY gantry system) and by including more data points, thus reducing the interpolation span and further increasing the accuracy of the master set. Moreover, the prediction fidelity could be further strengthened by including additional features beyond the S_{21} gain and phase magnitude. These will be subjects of follow up work.

Resonance Frequency Normalization

Another useful application of this new method is to use the position prediction to normalize the positional-dependent signal of embedded resonant sensors. Examples of this are sensors for soil health in which the sensor is buried and scanned throughout a growing season or sensors embedded within bandages for wound monitoring. Using our measurement setup, the frequency of a sensor can modulate over 1 MHz solely based on changes in X, Y, or θ position (Supplement 3). Thus to get an improved measurement of sensor response, we must take into

account the change in resonant signal caused by position changes and correct based on the measured positional change.

We test this application by placing an additional resonator below the center of the positional resonator array (Figure 5a); we then collect signal master data for interpolation, observing the change in measured resonant frequency from the center resonator based on position changes. The center resonator is designed to interact with a desired analyte (a sensor) whereas the four resonators above are shielded from this analyte effect (by keeping a 21 mm air gap between them) and are used to predict the reader's position, thereby enabling normalization of the sensor signal (Figure 5b). In this study, the center resonant sensor responds to water volume and four flyby trajectories are gathered at different water volumes. The signals collected along these trajectories were then normalized to a reference coordinate (x and y at 8 cm, and $\theta = 0°$) and compared to the actual resonant frequency obtained at that reference coordinate (Figure 5c). When the center sensor can be measured at multiple points along the trajectory, the resulting normalized signal is averaged. A transfer function for the 'true' response of the sensor is gathered by fitting the signal at the reference points with a 4 parameter logistics curve (5c insert). The sensor signal from the uncorrected and corrected flyby measurements are then compared to this reference transfer function and we find a 47% reduction in sum squared residual error when using the frequencies normalized based on the position prediction (Table 2). Three different trials of this experiment were completed (adding 0 to 2 mL water to the center sensor and scanning in four trajectories). The residuals for each run is plotted (Figure 5d). These are calculated by finding the difference between the predicted, normalized sensor response and that of the reference measured at the center point.

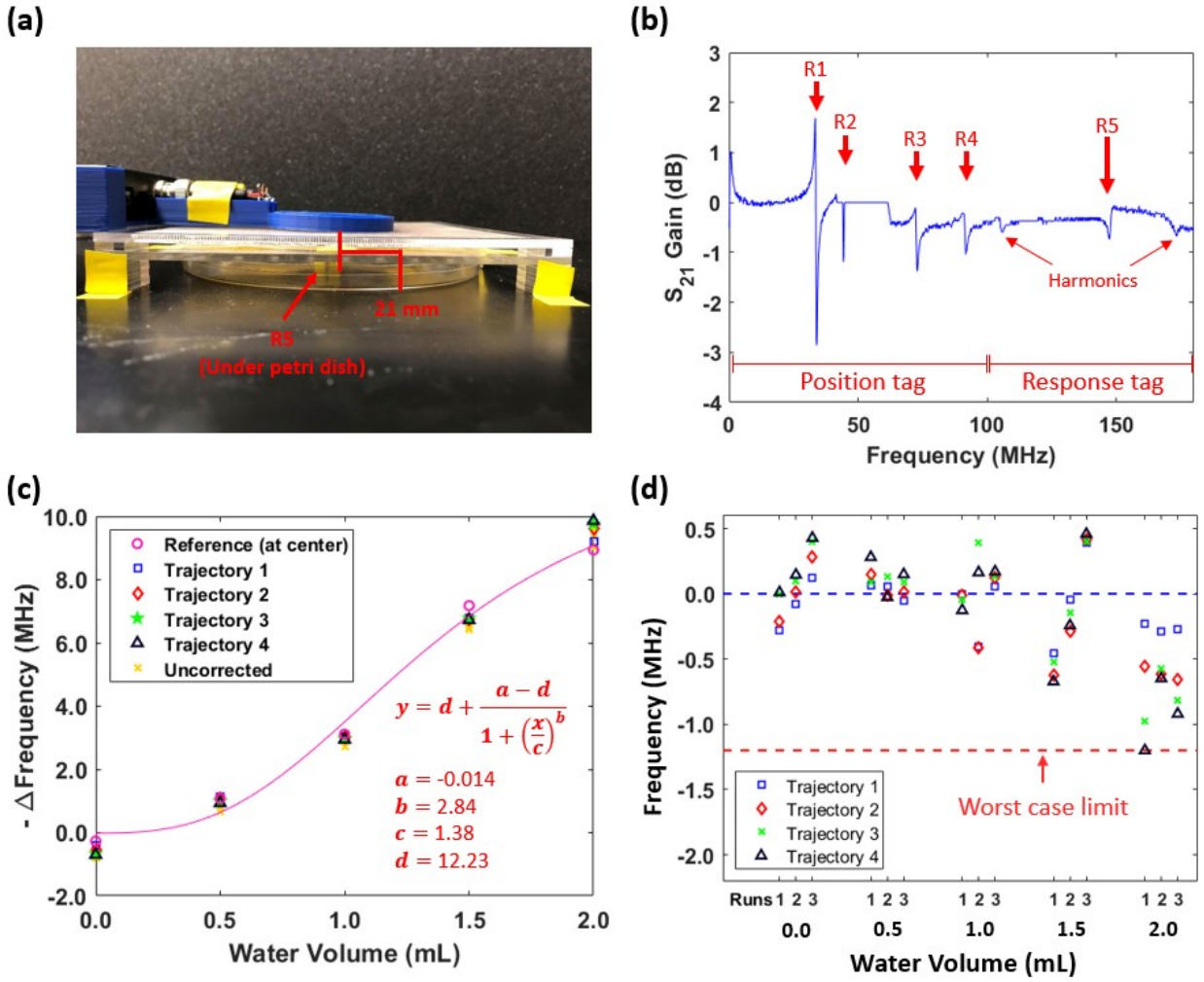

Figure 5 – Resonator array used to normalize response of embedded resonant sensor. (a) Side view of experimental setup where a circular spiral resonant sensor was placed underneath a petri dish and the setup from Figure 1c. (b) Scattering response resulted from all five resonators with arrow indicating the center resonant sensor peak, or 'response tag'. (c) Normalized frequency from trajectories 1, 2, 3, and 4 (labeled in Figure 4a) shown with the uncorrected signals from each trajectory and the 'true' center reference signal at different water volumes. The 'true' center reference signal is fitted with a four parameter logistic curve with the parameters shown in red. (d) Residual plot showing frequency difference between predicted sensor reading and actual sensor reading (referenced as center measurement) for both corrected and uncorrected measurements. Blue line represents the best case where there is no difference between normalized and actual signals whereas red line represents the worst case that the signal could differ without normalization.

Table 2 – Residual sum of squares between the four parameter logistic curve fitting of the center reference signal (true transfer function) and that of each trajectory, before normalizing and after normalizing.

Trajectory	Residual sum of squares
Uncorrected 1	20.56

Uncorrected 2	19.00
Uncorrected 3	14.23
Uncorrected 4	19.23
Normalized 1	4.86
Normalized 2	7.28
Normalized 3	9.17
Normalized 4	11.30

A few observations can be drawn from the residual plot (Fig 5d). First, for this sensor, lower water volumes are more reproducible, showing an average residual (averaging the four trajectories for each run) of 0.04 to 0.15 MHz for each of the runs at 0.5 ml water volume. The error gets larger as the volume increases, with an average residual of -0.53 to -0.74 MHz for the runs at 2 mL. Two possible reasons have contributed to this error. First, there is variability in how the larger volumes of water spread across the hydrophobic sensor surface, which could be mitigated in future sensor designs with more controlled, water wicking materials or a fluid channel to direct the water. Second, the sensor master calibration data, that is how the center resonator signal changes dependent on position, is taken with the resonator in air. Since the sensor response signals were normalized using only this air calibration data, it logically follows that the correction error increases as the measurement condition deviates further from the calibration conditions. This will be mitigated by obtaining multiple calibration data sets at various sensor response states (again with a more accurate, automated system). In an embedded, real-use system the resonant frequency would indicate the most suitable calibration set to use. For instance, if the signal from the center sensor is shifted by 20 MHz, calibration data that has the resonant frequency closest to the shifted frequency would be used to normalize the signal. This should reduce the error observed from higher water volume conditions. In all cases the signal found by position correction and averaging using multiple trajectories shows closer relation to the reference signal in comparison to the uncorrected signal (Table 2). The collection of multiple 'fly-by' measurements could be practically realized by an automated reader that drives over an embedded resonant sensor with a few different linear trajectories (like a field robot passing over the buried sensor).

Another practical constraint to test for this proposed system is the ability to isolate the signals of the positional resonator array from the analyte that will cause a change to the center sensor. In the case of a ground water sensor, this means the positional array should not be affected by changes in water level while still allowing the center sensor to be affected. In this initial, bench-top, controlled-environment work the 2.1 cm air gap between the position resonator array and the center sensor resonator was sufficient to isolate the resonator array from changes in water. We have tested this same strategy to shield the position array against water response in buried

soil by covering the positional array with a 3D-printed lattice work of polylactic acid (PLA) and a water impervious coating (nitrocellulose). A small channel can still direct the fluid of interest to the sensor. Simply increasing the lattice height on the sensor can shield all effects of increased water content in the soil on the positional array resonant frequencies, with a 1.9 cm height sufficient to shield all effects (Supplement 8). However, this does increase the step-off distance between the embedded resonators and reader. We have found that the resonator signal is clear above reader noise up to a 3 cm step-off distance (Supplement 9). This distance could be further improved by optimizing our reader and sensor geometry and by increasing the power of the portable reader. Moreover, the shielding thickness might be further reduced by changing the material used to shield the positional array.

Conclusions

In this work we demonstrate the use of a resonant array to accomplish wireless positional sensing, resolving both x-y location and angle. We found that with our manually-collected, interpolation data we can achieve an accuracy of 3.2 mm in x and y and 1.5° in angular. This could be further improved by collecting the master calibration data with an automated system, including more resonators in the array, or by increasing the number of S_{21} features that are used in the algorithm. We have also demonstrated one useful application of such positional sensing for normalizing the response of an embedded resonant sensor which is highly sensitive to position and orientation. In its current state, the approach can correct sensor response to the range of 200-500 kHz for sensor conditions that closely match calibration data and up to 1 MHz for responses that deviate further away. It is also currently limited to step off distances of ~3 cm, which could be further increased by optimization (impedance matching) of the reader antenna and/or boosting the reader power. This work shows the first demonstration of reading resonant sensors using an inexpensive (<$400) portable VNA. Further applications of this positional sensing could include asset tracking or monitoring personnel in closed environments with no clear line of site. It could also be used for feedback control in untethered soft robotics. The small array used herein could be readily applied on a larger surface area by embedding the 2x2 array onto structural materials that are then arrayed onto larger surfaces, such as floor tiles. As long as the resonator pattern is tessellated the algorithm could be readily extended to these larger surfaces.

Materials and Methods

Resonator fabrication

Four square spirals with pitch sizes of 1.2, 1.5, 2.5, and 3mm were designed in Rhinoceros ® 5 software. These designs were written as mask on Pyralux (copper coated polyimide) sheets using an indelible marker and an X-Y plotter (Curio printer). After air-drying for 1hr, the Pyralux sheets were submerged into solution containing 2:1 ratio of 3 wt% hydrogen peroxide and 31.45 wt% hydrochloric acid. Once the unmasked copper is etched away (approximately 10 minutes, observed by eye), the sample is removed and rinsed with water. Acetone is then used to remove the sharpie traces. The sample is again rinsed with water and allowed to air-dry. A circular spiral resonator was also designed with pitch size of 3mm and was fabricated using the same procedures above for the center sensor. The four square spiral resonators resulted in resonance frequency of around 30, 45, 70, and 90MHz, respectively, whereas the circular spiral resonator resulted in resonance frequency of around 150MHz.

Reader and Signal Acquisition

An inexpensive, portable vector network analyzer (Metrovna Deluxe) was used to capture the scattering parameters—S_{21} gain and S_{21} phase—over a range of 0.1MHz to 180MHz. Each of the two ports of the VNA was connected to a copper loop with a diameter of 5.4 cm through soldering the copper coils onto BNC wires, as shown in Figure 1b. Another wire connection was made in between the two copper coils to mutually ground the system. A holder was designed to support the reader system and was 3D-printed in acrylonitrile butadiene styrene (ABS). When taking measurements, the VNA was connected to a Raspberry Pi 3 through Bluetooth and the VNA/J software was used to interrogate the VNA to collect signals. The signal for each measurement was background subtracted where the background signal was taken without resonators present. For gain data, the background subtraction was done by calibration in the VNA/J program; for phase data, the background subtraction was done during data analysis in Matlab.

Experiment Setup and Data Collection

Two acrylic sheets (160x160x3 mm) were laser cut using (GlowForge ® Plus). One of them was engraved with 1 cm interval grids, as shown in Figure 1a, and the other was engraved with 1 mm interval grids. The four fabricated resonators were taped onto the 1cm grids acrylic and the 1 mm gridded acrylic was placed on top with smaller pieces of acrylic (20x10x3 mm) as standoff legs, see Figure 1c. Five more of the standoff legs were stacked and supported on the bottom side to create room for the resonant sensor. For positional accuracy studies, measurements were taken at every 1 cm interval in X-Y direction (from 0 to 14 cm) as well as at every 10° interval in θ direction. For trajectory experiment, six samples were taken while moving the reader along each of the eight paths, as shown in Figure 4a. For sensor signal normalizing experiments, the circular spiral resonator was taped under a petri dish and then located below the center of the setup. Measurements were also taken similar to above, but only from 4 to 10 cm in the X-Y axes with the same intervals in X, Y, and θ directions. Six samples along trajectories 1, 2, 3, and 4 were taken just as in trajectory experiment when the petri dish was dry. Then, this step was repeated after adding 0.5, 1.0, 1.5, 2.0 mL of water in the proximal center of the petri dish.

Position Predicting Algorithm

A schematic for the position predicting process is shown in Figure 2. From the collected set of data, the top and bottom peaks of gain and phase were extracted using the built-in *findpeaks()* function in MATLAB. The peaks were then stacked onto a magnitude versus frequency plot to define the frequency region for each resonator. A peak prominence versus frequency plot was also produced and used to define the frequency regions when the observed noise was less than that of the peak magnitude data (Supplement 4). From these plots, the frequency ranges where the resonators reside were determined to be 32 to 38MHz for R1, 42 to 50MHz for R2, 68 to 80MHz for R3, and 88 to 100MHz for R4. These ranges were set slightly more than the observed frequency range to provide some tolerance for peak shifts. Once these frequency regions were defined, the peak with highest magnitude was selected from each region. This step was done for both top and bottom peaks in each gain and phase domain. Once the peak magnitudes in all frequency regions were archived for each coordinate, *interp3()* function was used to interpolate the signals down to 0.1 cm interval in the X-Y direction and 1° interval in the θ direction. Cubic interpolation was found to interpolate the parameters more accurately compared to linear. Similarly, this was done on top and bottom peaks of gain and that of phase. This was then saved as the master data table needed for position determining.

To predict the position of a new, 'unknown' sample, the top and bottom peaks with highest magnitude were extracted from each frequency region as detailed above. These magnitudes were then subtracted to the pre-saved data to determine error. To combine the error in gain and phase domain, those magnitude differences were divided by the peak magnitudes of each gain and phase domain for scaling. These were added together as the final error for each possible position. The predicted position is then reported by minimizing this error.

Fitting Algorithm

Six samples were taken along a linear path and the position predicting algorithm (above) was sued at each location. The 2000 positions with smallest error were saved for each sample. A pseudocode for how these 2000 positions at 6 different locations (12,000 predicted points) are pooled to improve positional accuracy is presented below and the code details are included in Supplement 5:

Part 1
Run interpolation algorithm to obtain the top 2000 positions for each sample

Part 2
For ∀ samples i
  For each of 2000 position j in sample i
    - Convert angle of position j into slope
    - Find intercept with the slope and the current x, y points
    - For all other positions that are not in sample i, eliminate the positions that has angle of ± 2° further away from current angle
    - For the remaining positions not in sample i, compute distance from the line
    - Eliminate positions that has their computed distance greater than a tolerance.
    - Save the remaining positions belonging to each sample

Part 3
For ∀ samples i
  - count the number of times of each coordinate appear in sample i obtained obtained from part 2.
  - sum up again with the count of neighbor coordinates (act like moving average).
  - archive the one third of coordinates with highest count
If combination of the highest count coordinates do not form a linear path
  - find the sample that is not following the trend
  - replace with the next highest count that is following the trend

Part 2 is a bottleneck and has a runtime of $O(m^2n)$, where m is number of samples taken along a path and n is the number of positions selected from each sample (2000 in this case). The operations within the for-loops of part 2 were significantly more efficient and were considered to take constant time. For applications where instantaneous result is desired, this part needs to be modified and further investigated.

Normalization

From the stacked bottom gain peaks versus frequency plot obtained above, the greatest value at each frequency was archived and further subtracted by 0.1 (as additional threshold). This creates a boundary such that when a detected signal at a particular frequency exceeds this boundary, it represents the signal of the sensor. Matlab code containing details for creating the boundary is included in Supplement 6. Data collection with center resonator was then passed through this filter and thus the peaks belong to the sensor were extracted. Boundaries were also created for top gain peaks, bottom phase peaks, and top phase peaks and the same steps were repeated for peaks extraction. However, since the positions

where peaks were detected from bottom gain signal were the most after passing through their filters, frequency signals from bottom gain peaks were used to normalize frequency. For positions without detected peak, minimum frequency among the detected peaks in all positions were substituted. The frequencies at each position was then interpolated down to every 0.1cm and 1° intervals in x-y (4 to 10 cm) and θ (0° to 359°) directions, respectively. This completed the data needed for frequency normalization.

During a trajectory, the collected samples were processed in two paths: (1) peak extraction within the four frequency regions determined from the square resonators and (2) peak extraction that exceeded the boundary. From (1), the location of the sample was predicted using the position predicting algorithm. From (2), peak from the response sensor, in this case the center resonator, was collected. These two conditions were combined such that if the predicted coordinate from (1) was within the area of interpolation and a peak was detected from (2), the frequency difference between the predicted coordinate and reference coordinate was subtracted to frequency of the detected peak. This completed the peak normalization of a sample. If more than one sample along a trajectory fulfilled these conditions, average of the normalized frequency was presented.

Acknowledgements

Funding for this project was provided by NSF Award #1827578.

References

[1] E. Birdsell, M. Allen, and J. Park, “Wireless Ceramic Sensors Operating in High Temperature Environments,” no. July, pp. 1–11, 2012.

[2] Y. Wang, Y. Jia, Q. Chen, and Y. Wang, “A passive wireless temperature sensor for harsh environment applications,” *Sensors*, vol. 8, no. 12, pp. 7982–7995, 2008.

[3] O. Akar, T. Akin, and K. Najafi, “A wireless batch sealed absolute capacitive pressure sensor,” *Sensors Actuators, A Phys.*, vol. 95, no. 1, pp. 29–38, 2001.

[4] A. Dehennis and K. D. Wise, “A double-sided single-chip wireless pressure sensor,” *IEEE*, no. 3, pp. 252–255, 2002.

[5] Z. You, J. Mills-Beale, B. D. Pereles, and K. G. Ong, “A Wireless, Passive Embedded Sensor for Real-Time Monitoring of Water Content in Civil Engineering Materials,” *IEEE Sens. J.*, vol. 8, no. 12, pp. 2053–2058, 2008.

[6] X. Huang *et al.*, “Materials and designs for wireless epidermal sensors of hydration and strain,” *Adv. Funct. Mater.*, vol. 24, no. 25, pp. 3846–3854, 2014.

[7] X. Huang *et al.*, “Stretchable, wireless sensors and functional substrates for epidermal characterization of sweat,” *Small*, vol. 10, no. 15, pp. 3083–3090, 2014.

[8] B. D. Wiltshire, T. Zarifi, and M. H. Zarifi, “Passive Split Ring Resonator Tag Configuration for RFID-based Wireless Permittivity Sensing,” *IEEE Sens. J.*, vol. PP, no. c, p. 1, 2019.

[9] A. M. Gargari and M. H. Zarifi, “Passive Matched Mushroom Structure for a High Sensitivity Low Profile Antenna-Based Material Detection System,” vol. 19, no. 15, pp. 6154–6162, 2019.

[10] K. G. Ong, C. A. Grimes, C. L. Robbins, and R. S. Singh, “Design and application of a wireless, passive, resonant-circuit environmental monitoring sensor,” *Sensors Actuators, A Phys.*, vol. 93, no. 1, pp. 33–43, 2001.
[11] J. B. Hoag, “THE ABSORPTION OF RADIO WAVES IN WATER,” *Science (80-.).*, vol. 90, no. 2334, pp. 277 LP – 279, Sep. 1939.
[12] K. Bao *et al.*, “A readout circuit for wireless passive LC sensors and its application for gastrointestinal monitoring,” *Meas. Sci. Technol.*, vol. 25, no. 8, 2014.
[13] S. Charkhabi, A. M. Beierle, M. D. McDaniel, and N. F. Reuel, “Resonant Sensors for Low-Cost, Contact-Free Measurement of Hydrolytic Enzyme Activity in Closed Systems,” *ACS Sensors*, vol. 3, no. 8, pp. 1489–1498, 2018.
[14] S. Charkhabi, Y. J. Chan, D. G. Hwang, S. T. Frey, M. D. Bartlett, and N. F. Reuel, “Kirigami-Enabled, Passive Resonant Sensors for Wireless Deformation Monitoring,” *Adv. Mater. Technol.*, vol. 4, no. 5, May 2019.
[15] R. Sarpeshkar, *Ultra Low Power Bioelectronics*. Cambridge University Press, 2011.
[16] J. Naqui, J. Coromina, A. Karami-horestani, and C. Fumeaux, “Angular Displacement and Velocity Sensors Based on Coplanar Waveguides (CPWs) Loaded with S-Shaped Split Ring Resonators (S-SRR),” pp. 9628–9650, 2015.
[17] R. Nopper, R. Niekrawietz, and L. Reindl, “Wireless readout of passive LC sensors,” *IEEE Trans. Instrum. Meas.*, vol. 59, no. 9, pp. 2450–2457, 2010.
[18] J. García-Cantón, A. Merlos, and A. Baldi, “A wireless LC chemical sensor based on a high quality factor EIS capacitor,” *Sensors Actuators, B Chem.*, vol. 126, no. 2, pp. 648–654, 2007.